Speed Sensorless Control of SPMSM Drives for EVs With a Binary Search Algorithm-Based Phase-Locked Loop

Xiaodong Sun, *Senior Member*, *IEEE*, Changchang Hu, Gang Lei, *Member, IEEE*,
Zebin Yang, Youguang Guo, *Senior Member*, *IEEE*, and Jianguo Zhu, *Senior Member*, *IEEE*

***Abstract*—This paper presents a new method to extract accurate rotor position for the speed sensorless control of surface-mounted permanent-magnet synchronous motors (SPMSMs), based on the back electromotive force (EMF) information. The concept of finite control set-model predictive control is employed, and its cost function is related to the back EMF. An optimal voltage vector is selected from several given voltage vectors by comparing their fitness values. Moreover, the position space is divided into four sectors, and the fitness of each sector boundary is calculated and compared. The rotor position is first located in the sector surrounded by two boundaries that minimize the cost function. Then the selected sector is split into two parts, and the binary search algorithm is applied to reduce the sector area to improve the accuracy of position estimation. To overcome the drawback of the back EMF-based sensorless scheme, an *I-f* startup method is employed to accelerate the motor to the desired speed. An experiment has been carried out to compare the performance of the proposed method and the conventional phase-locked loop (PLL) in terms of steady-state and transient conditions.**

***Index terms*- Binary search algorithm, sensorless control, phase locked loop (PLL), surface-mounted permanent-magnet synchronous motor (SPMSM).**

I. INTRODUCTION

DUE to the worldwide environment deterioration, the improvement of energy efficiency has become increasingly important. Compared to traditional internal combustion engine vehicles, electrical vehicles (EVs) have higher energy efficiency and lower emissions. With the advantages of high-power density, robustness, high efficiency, large torque to inertia ratio and better controllability, the permanent magnet synchronous motors (PMSMs) are considered more suitable for EV applications [1-4].

The PI-based field-oriented control (FOC) system has been widely employed for PMSMs. It usually uses encoders or transducers to obtain rotor position information. Hence, the encoders and transducers need to be precisely installed, which will greatly increase the system cost [5], [6]. In recent years, various sensorless strategies have been developed to overcome this problem. These strategies can be divided into two categories, i.e., the saliency tracking-based methods and the fundamental model-based methods [7].

The saliency tracking-based methods usually inject some kinds of high-frequency (HF) signals to the PMSM and the rotor position is estimated according to the rotor saliency (i.e. the difference between the *d*–axis and *q*–axis inductances). They can work at very low-speed range and even at standstill. Moreover, they can work without motor parameters. The HF injection method is widely used in interior permanent magnet synchronous motors (IPMSMs) [8-16]. However, due to the lack of saliency, this method is not suitable for surface-mounted permanent magnet synchronous (SPMSMs).

Although the saliency tracking-based methods have attractive performance, the signal injection could cause extra losses, torque ripple and transient disturbances. Modifications of the drive system hardware are always required for these methods, which makes them difficult to be implemented in industrial applications. The fundamental model-based methods usually extract rotor positions from motor flux or back electromotive force (EMF). This kind of method has advantages of simplicity and straightforwardness [17-25]. In this category, there are various approaches to obtain rotor position information. In [17], the rotor position and speed wer estimated by a sliding mode observer (SMO). In [18], the sliding-mode coefficients were tuned by an adaptive algorithm online. Thus, the position estimation error caused by voltage source inverter (VSI) nonlinearity can be reduced. In [19], a full-order SMO was designed to obtain the extended EMF (EEMF). Compared to the EMF, the EEMF can be detected even at extremely low speed. The sensorless scheme based on EEMF can reverse

Manuscript received September 24, 2019; revised January 7, 2020 and February 9, 2020; accepted March 11, 2020. This work was supported by the National Natural Science Foundation of China under Project 51875261, the Natural Science Foundation of Jiangsu Province of China under Projects BK20180046 and BK20170071, the "Qinglan project" of Jiangsu Province, the Key Project of Natural Science Foundation of Jiangsu Higher Education Institutions under Project 17KJA460005, the Six Categories Talent Peak of Jiangsu Province under Project 2015-XNYQC-003, and the Postgraduate Research & Practice Innovation Program of Jiangsu Province under Project SJCX18_0745. *(Corresponding author: Gang Lei.)*

X. Sun and C. Hu are with the Automotive Engineering Research Institute, Jiangsu University, Zhenjiang 212013, China (email: xdsun@ujs.edu.cn, huchangchang_jd@163.com).

Z. Yang is with the School of Electrical and Information Engineering, Jiangsu University, Zhenjiang 212013, China (e-mail:zbyang@ujs.edu.cn).

G. Lei and Y. Guo are with the School of Electrical and Data Engineering, University of Technology Sydney, NSW 2007, Australia (e-mail: Gang.Lei@uts.edu.au, Youguang.Guo-1@uts.edu.au).

J. Zhu is with the School of Electrical and Information Engineering, University of Sydney, NSW, 2006, Australia (e-mail: jianguo.zhu@sydney.edu.au).

motor speed without any position sensor. In addition to the SMO, the other observers like Luenberger observer (LO) [20], extended Kalman filter (EKF) [21-23], and model reference adaptive system (MRAS) [24], [25] were also employed for position estimation.

However, additional approaches are needed to extract rotor position and speed information from the estimated back EMF. Conventionally, the position can be calculated directly from back EMF through an arctangent function. The estimation accuracy may be seriously affected by the noise and harmonics, so the phase-locked loop (PLL) approaches are employed to obtain rotor position in most of the fundamental model-based sensorless schemes.

To improve the performance of PLLs, different methods to augment PLL have been proposed in [26-34], and their advantages have been explored. In [26], an arctangent calculation was cascaded to the conventional PLL to eliminate the small-signal approximation caused by the sinusoidal distribution of back-EMF voltages. In [27], a generalized PLL was designed for all kinds of electrical machines. This PLL consists of a basic PLL and a feedforward signal path. In [28], the author proposed a PLL developed in synchronous rotating frame to evaluate rotor position and speed for predictive deadbeat control. Except the synchronous rotating frame, this PLL structure seems very similar to the conventional one. In [29], another attempt was made to combine model predictive current control (MPCC) with a sensorless scheme. The novel second-order PLL proposed in this work has a relatively high bandwidth and acceptable robustness against high-frequency disturbances and parameter errors. While this second-order PLL also consists of a plant model, fixed coefficients proportional controller and integral controller. In [31], the author presented a rotor position detection method for SPMSMs that can work in a wide speed range. The controller structure in this work combines the PLL with a PD controller and a lowpass filter. In [33], authors developed a sensorless scheme for PMSM which have good robustness and can suppress harmonics within a large range of speed. In this method, two synchronous frequency-extract filters (SFFs) were developed to improve the performance of conventional orthogonal PLL.

As mentioned above, it can be concluded that a large amount of effort has been made to extend the working speed range of PLL and improve its robustness. However, these PLLs have a similar structure, i.e. the plant model to calculate back EMFs and several regulators with fixed coefficients that need to be tuned according to the application. This tuning process is mostly realized by trial and error, which is a very time-consuming process. Moreover, the fixed-parameter controllers cannot guarantee a satisfactory performance due to the variations of the motor parameters and working conditions. In this work, a PLL structure with no fixed-gain controller is proposed to overcome the drawbacks caused by the structure of the conventional PLL.

In the finite control set-model predictive control (FCS-MPC) for PMSMs, the inner current PI loop is replaced by the MPC controller, and it is designed to output the voltage vector that minimizes the cost function directly. Thus, the fixed-gain PI controllers are omitted. Compared to traditional PI controllers, FCS-MPC controllers have great advantages in fast response and constraints handling [34-40].

In this paper, the FCS-MPC concept is employed to eliminate all the fixed-gain controllers in conventional PLLs, and a binary search algorithm based PLL (BSA-PLL) is applied to different motors without any parameters to adjust. Similar to the FCS-MPC motor drive, the rotor position is obtained by selecting the best angle that can minimize the cost function. To facilitate position estimation, the rotor space is firstly divided into four sectors, and the rotor will be roughly located according to the fitness of sector boundaries. Then the sector will be further reduced by a binary search algorithm. The cost function of the proposed BSA-PLL is related to the back EMF. Moreover, to startup the surface-mounted permanent-magnet synchronous motors (SPMSMs), an *I-f* method is employed.

The remainder of this paper is organized as follows. Section II describes the sensorless control of SPMSMs with back EMF-based method. Section III details the principle of the proposed BSA-PLL. Section IV proposes a startup strategy. Section V presents the experimental results in four different working conditions, followed by the conclusion.

II. Sensorless Control Based on Back EMF

Fig. 1 shows the block diagram of a conventioanl back EMF-based sensorless vector control for the SPMSM drive. In the figure, $\widehat{\theta_e}$ is the estimated rotor position, and $\widehat{\omega_e}$ is the estimated rotor speed in electrical. The vector control scheme consists of two cascaded control loops, i.e., the outer speed loop and the inner current loop. The inner current control loop is used to regulate the *d*- and *q*- axis currents of the SPMSM, and the controllers in this loop output the control voltage u_d and u_q. The outer controller is employed to generate the reference current in *q*-axis in terms of the errors between the reference and actual rotor speeds. In the sensorless case, the actual speed ω_e will be replaced by the estimated speed $\widehat{\omega_e}$. The inner current controllers are implemented in the synchronous rotating frame, so the rotor position needs to be observed exactly.

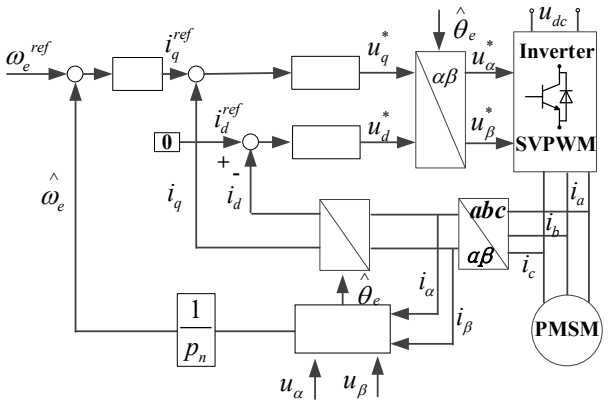

Fig. 1. Sensorless control scheme for SPMSM.

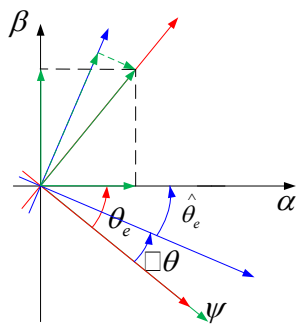

Fig. 2. Vector diagram of the synchronous frame.

Fig. 2 shows the space vector diagram of the synchronous rotating frame, where the actual *d*-axis is aligned with the permanent-magnet flux linkage [41], [42]. The γ-δ frame is the estimated synchronous rotating frame. In the figure, e_s is the back EMF, e_d and e_q are orthogonal components of the back EMF on the estimated *d*-, *q*- axis, θ_e and $\Delta\theta$ are the actual rotor position and the error between the actual and the estimated rotor position, respectively. When $\Delta\theta$ is small enough, it can be assumed that $\Delta\theta \approx e_d$. Therefore, e_d can be employed as an indicator to show the accuracy of the estimated rotor position. For this purpose, the back EMF must be calculated first, and a discrete-time model is required. Using the forward Euler method and taking *Ts* as the sample time, the discrete form of SPMSM model in the stationary frame can be written as

$$\begin{cases} L_s \dfrac{i_\alpha(k+1)-i_\alpha(k)}{Ts} = u_\alpha(k) - R_s i_\alpha(k) - e_\alpha(k) \\ L_s \dfrac{i_\beta(k+1)-i_\beta(k)}{Ts} = u_\beta(k) - R_s i_\beta(k) - e_\beta(k) \end{cases} \tag{1}$$

where L_s is the stator inductance, i_α (*t*) and i_β (*t*) are the α-axis and β-axis stator currents, respectively, u_α (*t*) and u_β (*t*) are the α-axis and β-axis stator voltages, respectively, e_α (*t*) and e_β (*t*) are the α-axis and β-axis back EMF of the SPMSM, respectively, R_s is the stator resistance, *k* is the current sampling instant, and *Ts* is the sample time. Thus, the back EMF can be calculated as

$$\begin{cases} e_\alpha(k) = u_\alpha(k) - R_s i_\alpha(k) - L_s \dfrac{i_\alpha(k+1)-i_\alpha(k)}{Ts} \\ e_\beta(k) = u_\beta(k) - R_s i_\alpha(k) - L_s \dfrac{i_\beta(k+1)-i_\beta(k)}{Ts} \end{cases} \tag{2}$$

After having obtained the back EMF in the stationary frame, the rotor position can be obtained directly by arctangent function

$$\theta_e(k) = \arctan \frac{e_\alpha(k)}{e_\beta(k)} \tag{3}$$

However, the accuracy of position estimation may be seriously affected by the existence of noise and harmonics, especially when the back EMF crosses zero. In order to overcome this problem, the PLL methods are always adopted to extract position signals from the back EMF. In [28], a PLL method in the synchronous reference frame (SRF-PLL) was employed to obtain position information. To construct the SRF-PLL, the SPMSM model needs to be rewritten in the synchronous reference frame

$$\begin{cases} u_\gamma(k) = R_s i_\gamma(k) + L_s \dfrac{\mathrm{V} i_\gamma(k)}{Ts} - L_s \omega_e(t) i_\delta(t) - \omega_e \psi \mathrm{V}\theta \\ u_\delta(k) = R_s i_\delta(k) + L_s \dfrac{\mathrm{V} i_\delta(k)}{Ts} + L_s \omega_e(t) i_\delta(t) + \omega_e \psi \end{cases} \tag{4}$$

where $u_\delta(t)$ and $u_\gamma(t)$ are the δ-axis and γ-axis stator voltages, respectively, i_δ (*t*) and i_γ (*t*) are the δ-axis and γ-axis stator currents, respectively, and ψ is the magnetic flux.

The machine velocity and angle are given by the δ-axis and γ-axis equations, respectively. The relative equations are

$$\omega_e(k) = \frac{u_\delta(k) - R_s i_\delta(q) - L_\delta \dfrac{\mathrm{V} i_\delta(k)}{Ts}}{L_\gamma i_\gamma(k) + \psi} \tag{5}$$

$$\Delta\theta(k) = \frac{-1}{\omega_e(k)\psi}\left(u_\gamma(k) - R_s i_\gamma(k) - L_\gamma \frac{\mathrm{V} i_\gamma(k)}{Ts} + \omega_e(k) L_\delta i_\delta(k)\right) \tag{6}$$

where $\mathrm{V} i_{\gamma\delta}(k) = i_{\gamma\delta}(k) - i_{\gamma\delta}(k-1)$

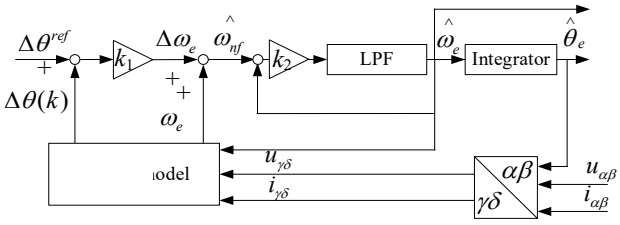

Fig. 3. Block diagram of the conventional PLL.

In Fig. 3, k_1 and k_2 are controller gains. $\Delta\theta^{ref} = 0$, is the expected error between the estimated reference frame and the real reference frame. $\Delta\theta$ is the error between the estimated reference frame and the real reference frame. It can be calculated from (6), and the PLL used to obtain rotor positions can be designed as in Fig. 3. As shown, the error between the calculated rotor position and the actual rotor position is used to generate the correct signal for the rotor position estimation. If $\Delta\theta$ is a positive number (as shown in Fig. 2), the actual rotor position is ahead of the assumed position, and thus the estimated motor speed should increase so that the assumed rotor position can catch up the real one. Therefore, it can be considered that the estimated synchronous reference frame is aligned with the rotor flux if the position error is kept small.

For this reason, the position error signal is amplified by a proportion controller as a compensation term $\Delta\omega_e$ for speed evaluation. And ω_e, the speed calculated directly from function (5), is treated as a feedforward term. Therefore, the obtained rotor speed before the filters ($\hat{\omega}_{nf}$) can be expressed as

$$\hat{\omega}_{nf} = k_1 \Delta\theta + \omega_e \tag{7}$$

In order to reduce the influence of high-frequency noise, a first-order filter is employed in this PLL structure.

$$\hat{\omega}_e = k_2 \int_0^t (\hat{\omega}_{nf} - \hat{\omega}_e) dt \tag{8}$$

where k_2 determines the bandwidth of the filter structure, and *t* is the instant of calculation. The discretization form of the above formula can be written as

$$\hat{\omega}_e(k) = k_2 Ts[k_1 \Delta\theta(k) + \omega(k) - \omega(k-1) + \hat{\omega}_e(k-1)] \tag{9}$$

After the rotor speed is calculated, the position can be obtained by integration as shown in Fig. 3.

$$\hat{\theta}_e = \int_0^t \hat{\omega}_e \, dt \tag{10}$$

Rewritten in the discrete form, it becomes

$$\hat{\theta}_e(k) = \hat{\theta}_e(k-1) + Ts\,\hat{\omega}(k) \tag{11}$$

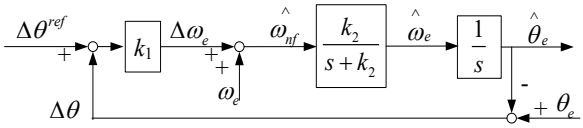

Fig. 4. Simplified structure of the conventional PLL.

For tuning of the coefficients in PLL, the conventional PLL can be simplified as shown in Fig. 4 [28], and the open-loop transfer function can be written as

$$G_{ol}(s) = k_1 \frac{k_2}{s+k_2}\frac{1}{s} \tag{12}$$

Various techniques can be employed to select the coefficients. In this work, the symmetrical optimum method [28] is employed to compute the PLL parameters.

III. Binary Search Algorithm Based PLL

The conventional SPMSM sensorless control scheme often utilizes a fixed gain PLL to extract rotor position signals from the back EMF. In this work, the principle of FCS-MPC is applied to obtain the rotor position.

In the FCS-MPC, future behaviors of the plant with different inverter switching states are predicted over a given prediction horizon. By comparing different future performances, the optimal inverter state in the next time can be selected. The comparison criterion is known as the cost function. Cost functions in PMSM control case are usually related to the dynamic responses and static performance of the motor drive, and the rotor speed or current vectors are often adopted to calculate them.

As mentioned above, the back EMF in the assumed *d*-axis can be treated as an indicator for the estimation accuracy. From (2), back-EMFs in the α and β axes can be obtained. The main reasons for not calculating rotor position directly by doing an arctan operation are that the accuracy of position estimation by arctan technique may be seriously affected by the existence of noise and harmonics, and arctan function performs not well especially when the back EMF crosses zero. In this paper, by applying Park transform with the assumed rotor position, the estimation error of the corresponding error can be obtained . Therefore, the cost function in this work is

$$J_i = 1000\times|\cos\theta_i \; e_\alpha(i) + \sin\theta_i \; e_\beta(i)| \tag{13}$$

where J_i is the fitness value of rotor position θ_i. Unlike the power inverters, rotor positions change continuously between 0 and 2π rad. In order to make comparisons with the proposed cost function, the position space needs to be divided into finite sectors. And the fitness of each border will be calculated and compared to explore the optimal rotor position. For improving the computational efficiency, the searching progress is implemented in a binary form. The flowchart of the proposed search algorithm is illustrated in Fig. 5 and the block diagram of the proposed BSA-PLL is shown in Fig. 6.

As illustrated in Fig. 5, the proposed search algorithm consists of three parts. The first part is the initialization. The process aims to provide the necessary information for the next binary cycle step, i.e., the initial value of θ_1, θ_2 and θ_m. The processes of determination are described as follows.

Step 1. Sampling the current and voltage in stationary reference.

Step 2. Calculate back EMF using (3).

Step 3. Define four preset positions using the estimated rotor position in the previous instant $\hat{\theta}_e(k-1)$. They are $\theta_0 = \hat{\theta}_e(k-1) + 0$, $\theta_{\frac{\pi}{2}} = \hat{\theta}_e(k-1) + \frac{\pi}{2}$, $\theta_{\pi} = \hat{\theta}_e(k-1) + \pi$ and $\theta_{\frac{3\pi}{2}} = \hat{\theta}_e(k-1) + \frac{3\pi}{2}$.

Step 4. Calculate the fitness values of the four preset positions using (13).

Step 5. Take the two positions with the smallest fitness as θ_1 and θ_2, respectively.

Step 6. Take θ_m as the median of θ_1 and θ_2. $\theta_m = \frac{1}{2}(\theta_1 + \theta_2)$.

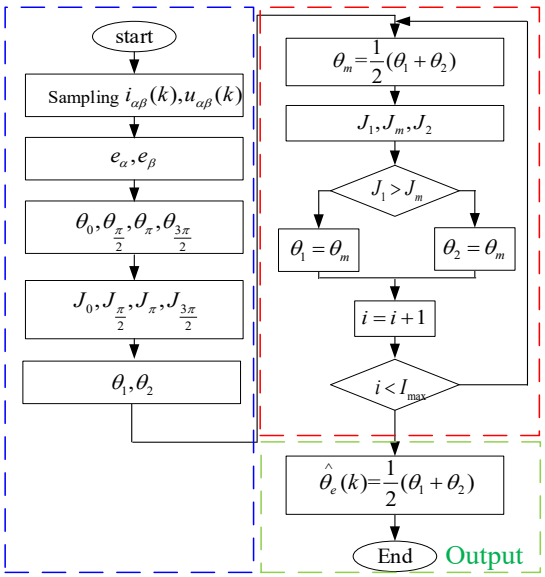

Fig. 5. Flowchart of the proposed search algorithm.

In Step 1, the previous rotor position is obtained by a unit delay of the proposed BSA-PLL output, as illustrated in Fig. 6. The position space is divided into four sectors firstly, as shown in Fig. 7. Then the real rotor position is roughly located in the sector between θ_1 and θ_2.

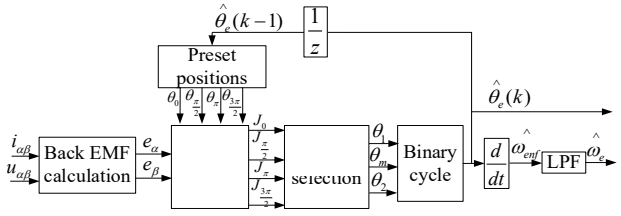

Fig. 6. Block diagram of the proposed BSA-PLL.

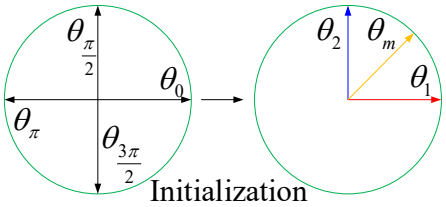

Fig. 7. Initialization process of position space.

The binary cycle is employed to locate rotor positions more accurately in the sector which is selected in the initialization part, as shown in Fig, 8, where *Imax* represents the maximum cycle. In each cycle, the sector will firstly be divided into two equal halves by θ_m, and the fitness of sector boundaries will then be compared with the fitness of the sector median. The boundary with a larger fitness value will be replaced by the median. Thus, the sector can be reduced to its half, and the accuracy of position estimation can be doubled.

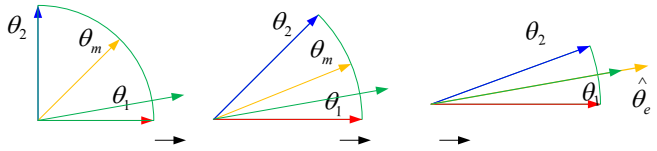

Fig. 8. Binary search process.

The selected sector becomes smaller with the increase of the binary cycle. After the maximum cycle is reached, the final estimated rotor position will be generated as the median of the last sector.

$$\hat{\theta}_e(k) = \frac{1}{2}(\theta_1 + \theta_2) \tag{14}$$

And the accuracy of the estimation is

$$Accuracy = \frac{\pi}{2} \times \frac{1}{2^{Imax+1}} \tag{15}$$

Due to the simplicity of the binary search algorithm, the processor can hold a relatively large maximum cycle. If the maximum cycle is set to 15, the accuracy of rotor position estimation will be 0.000024 rad. Therefore, the proposed BSA-PLL can estimate the rotor position with high precision.

After the rotor position is obtained, the rotor speed can be calculated by differentiating the position. In discrete form, it can be written as

$$\hat{\omega}_{enf} = \frac{\hat{\theta}_e(k) - \hat{\theta}_e(k-1)}{Ts} \tag{16}$$

Since there exists high-frequency noise, an LPF is employed to filter this signal, and the final estimated rotor speed can be obtained, as shown in Fig. 6. Compared to the traditional PLL, the main feature of the proposed BSA-PLL structure is the absence of fixed gain controllers. This feature makes it possible to avoid the effort on adjusting controller parameters. Without any parameters to be tuned, the proposed BSA-PLL can be extended to any other PMSMs directly. The high-efficiency speed range of the motor is 300-400 rpm. The estimated rotor positions in each iteration when rotor at 1.5 rad with 200 rpm and 2 rad with 350 rpm are listed in Table I and Table II, respectively. The bold number stands for the updated boundary.

TABLE 1. ESTIMATED ROTOR POSITIONS IN EACH ITERATION AT 200RPM

Iter	θ_1	Measured	θ_2	error
1	1.495457	1.500000	**3.066253**	0.780855
2	1.495457		**2.280855**	0.388156
3	1.495457		**1.888156**	0.191807
4	1.495457		**1.691807**	0.093632
5	1.495457		**1.593632**	0.044544
6	1.495457		**1.544545**	0.020001
7	1.495457		**1.520001**	0.077293
8	1.495457		**1.507729**	0.015934
9	1.495457		**1.501593**	0.001474
10	**1.498525**		1.501593	0.000059
11	1.498525		**1.500059**	7.075025
12	**1.499292**		1.500059	3.240073
13	**1.499676**		1.500059	1.322597e-04
14	**1.499867**		1.500059	3.638593e-05
15	**1.499963**		1.500059	
$\hat{\theta}_e$		1.500012		1.155096e-05

TABLE II. ESTIMATED ROTOR POSITIONS IN EACH ITERATION AT 350RPM

Iter	θ_1	Measured	θ_2	error
1	1.99205	2.00000	**3.562846**	0.777448
2	1.99205		**2.777448**	0.384749
3	1.99205		**2.384749**	0.1884
4	1.99205		**2.188400**	0.090225
5	1.99205		**2.090225**	0.041137
6	1.99205		**2.041137**	0.016594
7	1.99205		**2.016594**	0.004322
8	1.99205		**2.004322**	-0.001814
9	**1.998186**		2.004322	0.001254
10	1.998186		**2.001254**	0.00028
11	**1.99972**		2.001254	0.000487
12	1.99972		**2.000487**	0.000103
13	1.99972		**2.000103**	8.83501E-05
14	**1.999912**		2.000103	7.52368E-06
15	1.999912		**2.000008**	
$\hat{\theta}_e$		1.99996		4.02382E-05

As indicated in the tables above, after the magnitude of the back EMF is sufficient to extract the rotor position, the iteration process and error of estimation are mainly related to the number of iterations rather than the speed.

IV. STARTUP STRATEGY

For the back EMF-based rotor position estimation method, the proposed BSA-PLL faces the problem of not being able to accurately extract the position signal due to the small back EMF at low speed. In this work, an *I-f* startup method is employed to start the motor without position sensors. The startup strategy includes two stages: the acceleration stage and the smooth transition stage [43].

A. Acceleration Stage

The purpose of the acceleration stage is to start the motor and accelerate it to a desired speed. In this stage, the reference speed increases in proportion to the time, while the current in δ-axis keeps invariable and the current in γ-axis is set to zero.

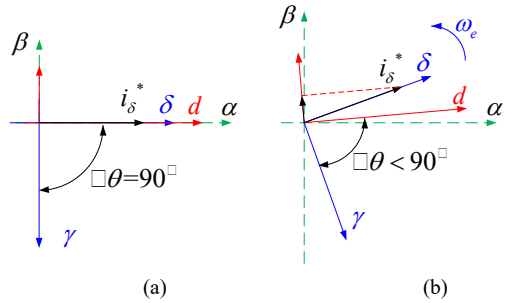

(a) (b)

Fig. 9. Vector diagram of the synchronous frame: (a) initial position, and (b) during acceleration.

The first step to startup is to align the *d*-axis in the synchronous reference frame and the α-axis in static reference frame together by applying dc currents to the motor. Then, the γ- axis is set to be lagging the *d*-axis by 90 electrical degrees, and thus the δ-axis can be aligned with the *d*-axis. Since the γ-axis current is set to zero, there is no current component on the *q*-axis at the beginning. Therefore, no torque will be generated, as illustrated in Fig. 9(a). However, when the $\gamma\delta$-reference frame starts to rotate due to the ramp speed command, the angle between δ-axis and *q*-axis will become smaller and current components will occur in *q*-axis.

$$i_q = i_\delta^* \cos \Delta\theta \tag{17}$$

The generated electrical torque can be calculated as

$$T_e = \frac{3}{2} p_n \psi i_q \tag{18}$$

where p_n is the number of pole pairs.

A self-stabilization mechanism exists in the acceleration stage. That is, if the load torque increases, the acceleration rate may decrease, and the lagging angle between *q*-axis and δ–axis will become smaller. Referring to (17), the current component in *q*-axis will be larger; consequently, as can be noted in (18), the motor will generate more electrical torque to balance the load torque. To maintain this self-stabilization mechanism, it is necessary to keep a relatively large lagging angle between the *q*-axis and δ-axis. Therefore, the current in δ-axis i_δ^* needs to be large enough, and it is related to the speed slope.

The ramp speed reference can be expressed as follows.

$$\omega_e = k_\omega t \tag{19}$$

Considering the mechanical model of SPMSM

$$\frac{d\omega_e}{dt} = \frac{p_n (T_e - T_L)}{J} \tag{20}$$

Combining (18), (19) and (20), we have

$$i_q = \frac{2}{3 p_n \psi} \left(\frac{J}{p_n} k_\omega + T_l \right) \tag{21}$$

In this work the safety angle between the *q*-axis and δ-axis is set to 45°, so the maximum current in *q*-axis i_q^* can be calculated as

$$i_q^* = i_\delta^* \sin 45^\circ \tag{22}$$

Thus the i_δ^* can be expressed as

$$i_\delta^* > \frac{2\sqrt{2}}{3 p_n \psi} \left(\frac{J}{p_n} k_\omega + T_{l,\max} \right) \tag{23}$$

where $T_{l,max}$ is the maximum load torque that the drive may experience during the startup.

B. Smooth Transition Stage

After the motor has accelerated to the desired speed, the amplitude of the back EMF is large enough to estimate the rotor position accurately. The sensorless FOC scheme is expected to switch in to take over the motor control. However, in order to ensure a reliable startup, the δ-axis current will be much larger than the *q*-axis current, so a direct switch to the FOC will cause high current and torque ripple. Therefore, before the transition, the δ-axis current needs to be reduced. When the torque generated by δ-axis current is close to the load torque, the two strategies can be safely switched from one to the other.

When the δ-axis current gets smaller, $\Delta\theta$ will be forced to decrease to maintain i_q constant. Therefore, $\Delta\theta$ can be selected as a threshold signal. In this research, the rotor position obtained by PLL is employed to take the real rotor position and the FOC will cut in when $\nabla\theta < 5^\circ$.

V. Experimental Results

To validate the effectiveness of the proposed sensorless control scheme, comparisons with traditional PLL (based on fixed-parameter PI) are carried out. These tests are conducted in dSPACE 1401 test bench. The experimental setup is shown in Fig. 10. The test bench consists of an SPMSM (a PM hub motor), a torque sensor, and a magnetic powder brake. Table III lists the parameters of the SPMSM. The experimental measurements are exported from the dSPACE platform to MATLAB and plotted.

TABLE III
Parameters of the SPMSM

Parameter	Symbol	Value	Unit
Stator resistance	R_s	0.8	Ω
Stator inductance	L_s	4.5	mH
No. of pole pairs	P	22	
Magnet flux	Ψ	0.215	Wb
Inertia	J_m	0.03	kgm^2
Frictional	B_m	0.0006	Nm/s
Rated speed	N	360	rpm
Rated power	P_N	3000	W

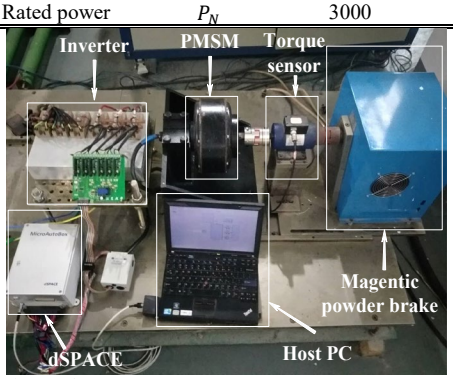

Fig.10. Experimental setup.

A. Startup and Transition Condition.

The switching speed is set to 200 rpm in this experiment. As shown in Fig. 11, the motor is accelerated from standstill to 200 rpm within 0.5 s. The speed slope is set to 750 and $i_\delta^* = 3.5\text{A}$.

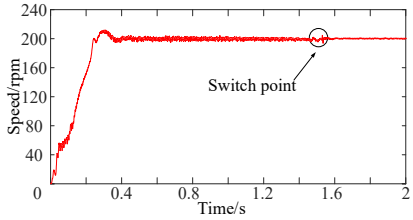

Fig. 11. Rotor speed in startup condition.

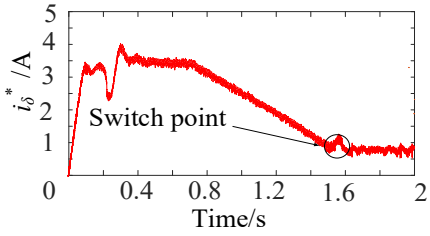

Fig. 12. Current i_δ^* during startup.

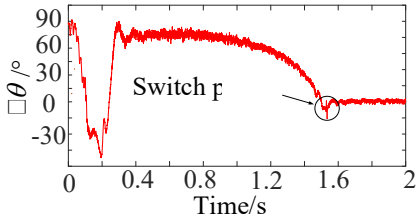

Fig. 13. Position error during startup.

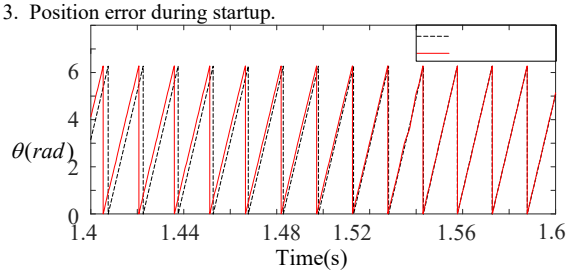

Fig.14 Estimated rotor position

Experimental results of the current in the synchronous rotating q-axis, the error between the synchronous rotating q-axis and the estimated rotor q-axis based on the back EMF and the rotor position obtained from estimation are shown in Figs. 12, 13 and 14, respectively. As can be observed from Figs. 12 and 13, the angle difference $\Delta\theta$ decreases with the decrease of i_δ, which is consistent with the previous prediction. It should be noted that the sensorless schemes are switched at about 1.5 s.

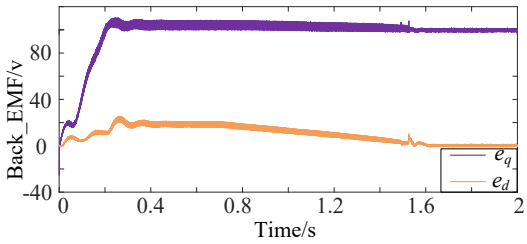

Fig.15 back EMF in d-q frame

As is shown in Fig.15, in the startup process, e_d has a non-zero amplitude, this may be caused by inaccurate rotor position. As the speed increases, the amplitude of e_q and e_d reach a stable value. The e_d starts to decrease in the gegaining of the smooth transition stage. In this stage, as can be seen in Fig.13 and Fig.14, the error of position estimation gradually decreases. After the switch point, the proposed BSA-PLL scheme takes over the control, the position can be estimated more precisely. Therefore, the ripples of back EMF are significantly reduced. Also, the amplitude of e_d drops to zero steadily after the switch point since the selected e_d -related cost function is meant to zero.

B. Comparisons with Traditional PLL at Steady State Condition.

In order to verify the steady-state performance of the proposed BSA-PLL, the results of the comparison test with the traditional PLL are recorded in Figs. 16-18.

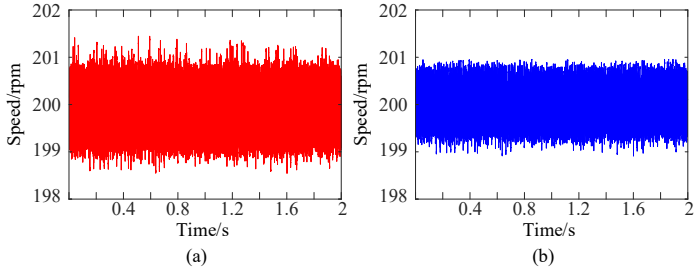

Fig. 16. Rotor speed at steady state: (a) proposed BSA-PLL, and (b) conventional PLL.

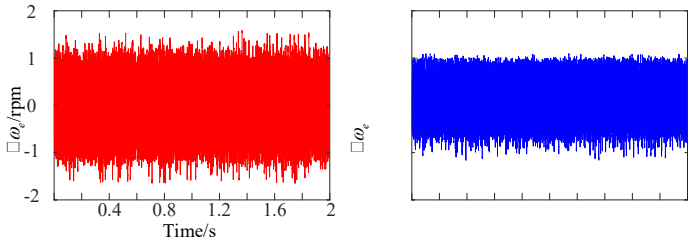

Fig. 17. Speed error at steady state: (a) proposed BSA-PLL, and (b) conventional PLL.

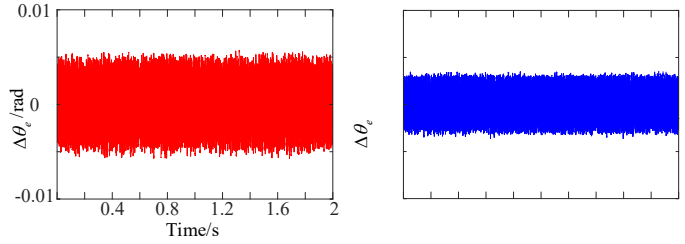

Fig. 18. Position error at steady state: (a) proposed BSA-PLL, and (b) conventional PLL

The reference speed is set to 200 rpm and load torque is 10 Nm. The plotted signals are the estimated speed, the error between the measured speed and estimated speed, and the error between the measured and estimated rotor positions, respectively. However, due to harmonics in the estimated back EMF and nonlinearities in power inverter, the accuracy of position estimation cannot reach the theoretical value. As can be observed from the above results, the proposed BSA-PLL will lead to a slightly higher ripple (about 9%) in the estimated speed than the conventional PLL. The performance is satisfactory.

C. Comparisons with Traditional PLL under Reference Speed Step Changing

The performance of both traditional PLL and the proposed BSA-PLL in transient condition are recorded in Figs. 19-21. In this condition, load torque is 10N m, and the rotor speed changes from 200 rpm to 350 rpm at the time t = 1 s, and the responses of the rotor speed, speed error, and rotor position error are illustrated in Figs. 19-21, respectively. As shown, when the reference speed step changes, neither the proposed BSA-PLL nor the traditional one can keep up with the change of speed in the first time (both $\Delta\omega_e$ in Fig.20 (a) and Fig.20 (b) are larger than zero in a short period after 1 s). However, compared to the proposed BSA-PLL, the traditional phase-PLL produces significant oscillations in the speed, speed error and rotor position error. The maximum error in $\Delta\omega_e$ with the proposed BSA-PLL is 5.8 rpm, while that with the conventional PLL is 15.3 rpm. Also, the proposed BSA-PLL takes about 0.2 s to minimize the speed error, while the traditional PLL takes about 0.35 s.

As for the rotor position error, the peak values of the two PLLs are similar, while the traditional PLL produces visible oscillations in the rotor position error and generates a slightly steady-state error after the reference speed step changes. However, the proposed BSA-PLL eliminates the rotor position error within a short time after 1 s; this may be due to the fact that there is no fixed-gain PI controller in the proposed BSA-PLL.

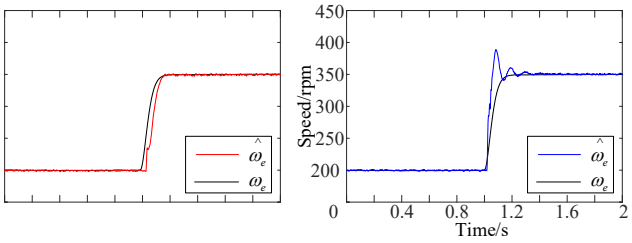

Fig. 19. Rotor speed at reference speed step changes condition: (a) proposed BSA-PLL, and (b) conventional PLL.

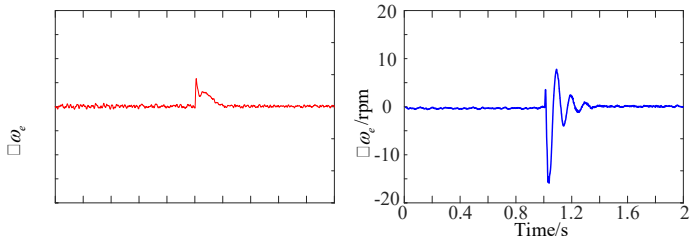

Fig. 20. Speed error at reference speed step changes condition: (a) proposed BSA-PLL, and (b) conventional PLL.

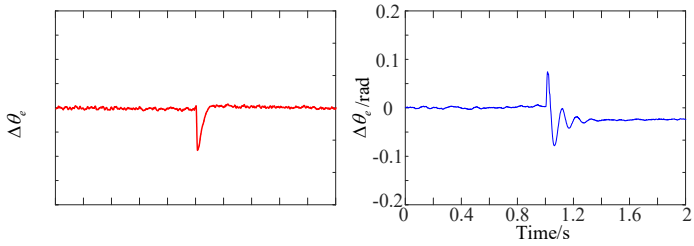

Fig. 21. Position error at reference speed step changes condition: (a) proposed BSA-PLL, and (b) conventional PLL.

D. Comparisons with Traditional PLL under Load Torque Step Changing

In this condition, the load torque step changes from 10 Nm to 20 Nm at t =1 s. The performance of the proposed BSA-PLL and the traditional PLL are recorded in Figs. 22-24.

Similar to the last case, the proposed BSA-PLL shows significant advantages in dynamic response. When the load torque changes, the proposed BSA-PLL is very effective in accurately estimating the rotor speed without any oscillations. As can be observed, the maximum speed error for the proposed BSA-PLL is 1.72 rpm, while it is -4.8 for the conventional PLL. Moreover, the time used to reduce speed error for the proposed BSA-PLL and the conventional PLL are about 0.3 s and 0.5 s, respectively. Moreover, although the ripple of position with the proposed BSA-PLL under steady-state is larger than that with the traditional PLL, the proposed BSA-PLL can reduce the position error by about 30% and the adjustment time by 40% when the load increases.

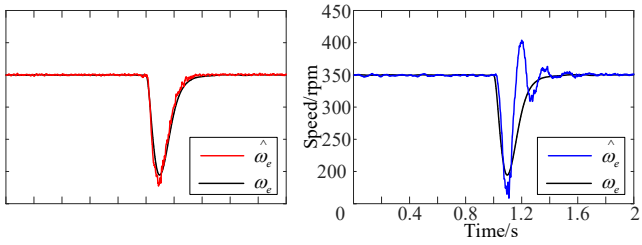

Fig. 22. Rotor speed at load torque step changes condition: (a) proposed BSA-PLL, and (b) conventional PLL.

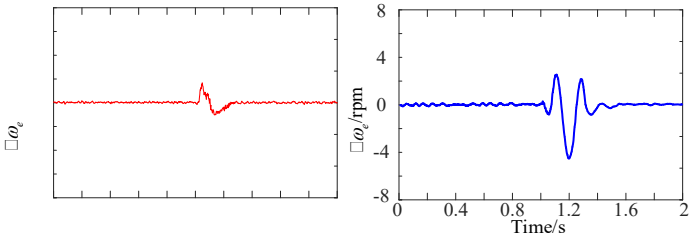

Fig. 23. Speed error at load torque step changes condition: (a) proposed BSA-PLL, and (b) conventional PLL.

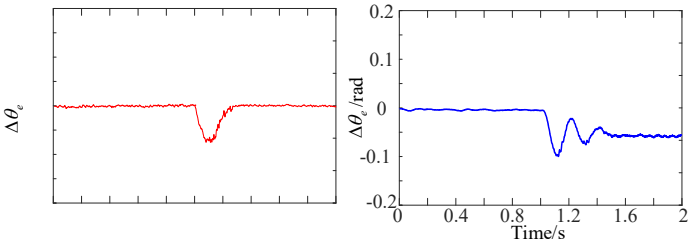

Fig. 24. Position error at load torque step changes condition: (a) proposed BSA-PLL, and (b) conventional PLL

Through the above analysis, the advantages of the proposed BSA-PLL in dynamic response are clearly illustrated.

VI. Conclusion

In this paper, a BSA-based PLL was proposed for the sensorless vector control of an SPMSM. Similar to the concept of the FCS-MPC, the position space of the proposed BSA-PLL was dived into four sectors and the finesses of each sector boundary was calculated. The cost function is related to back

EMF. The rotor position was roughly located in the sector which its boundaries minimize the cost function. To acquire a more accurate estimation, this sector was split into two parts and the part with the better fitness was selected. The rotor position can thus be located with good accuracy after several cycles. There is no fixed-gain PI controller in this PLL structure, and this makes it possible to avoid the effort on adjusting controller parameters. Experiments were carried out to compare the performances of the proposed BSA-PLL and the conventional PLL in both steady-state and transient conditions. Experimental results highlight the advantages of the proposed BSA-PLL, like faster response and smaller oscillations in speed and position estimation. The proposed BSA-PLL method can be extended to any other PMSMs directly without any extra work.

REFERENCES

[1] X. Sun, et al., "Core Losses Analysis of a Novel 16/10 Segmented Rotor Switched Reluctance BSG Motor for Hevs Using Nonlinear Lumped Parameter Equivalent Circuit Model." *IEEE Trans. Magn.*, vol. 23 no. 2, pp. 747-757, 2018.

[2] X. Sun, K. Diao, G. Lei, L. Chen, Y. Guo and J. Zhu, "Study on Segmented-Rotor Switched Reluctance Motors with Different Rotor Pole Numbers for BSG System of Hybrid Electric Vehicles," *IEEE Trans. Veh. Technol.*, vol. 68, no. 6, pp. 5537-5547, Jun. 2019.

[3] X. Sun, C. Hu, G. Lei, Y. Guo, and J. Zhu. "State Feedback Control for a PM Hub Motor Based on Grey Wolf Optimization Algorithm." *IEEE Trans. Power Electron*, vol. 35, no. 1, pp. 1136-1146, Jan. 2020.

[4] S. Fartash Toloue, S. H. Kamali and M. Moallem, "Torque Ripple Minimization and Control of a Permanent Magnet Synchronous Motor using Multi-objective Extremum Seeking," *IEEE/ASME Trans. Mechatronics*., doi: 10.1109/TMECH.2019.2929390

[5] Y. Mao, S. Zuo and J. Cao, "Effects of Rotor Position Error on Longitudinal Vibration of Electric Wheel System in In-Wheel PMSM Driven Vehicle," *IEEE/ASME Trans. Mechatronics*., vol. 23, no. 3, pp. 1314-1325, June 2018.

[6] S. K. Kommuri, S. B. Lee and K. C. Veluvolu, "Robust Sensors-Fault-Tolerance With Sliding Mode Estimation and Control for PMSM Drives," *IEEE/ASME Trans. Mechatronics*., vol. 23, no. 1, pp. 17-28, Feb. 2018.

[7] W. Xu, Y. Jiang, C. Mu, and F. Blaabjerg, "Improved nonlinear flux observer-based second-order SOIFO for PMSM sensorless control," *IEEE Trans. Power Electron*, vol. 34, no. 1, pp. 565-579, Jan. 2019.

[8] X. Luo, Q. Tang, A. Shen, and Q. Zhang, "PMSM sensorless control by injecting HF pulsating carrier signal into estimated fixed-frequency rotating reference frame," *IEEE Trans. Ind. Electron.,* vol. 63, no. 4, pp. 2294-2303, Apr. 2016.

[9] J. Lu, Y. Hu, X. Zhang, Z. Wang, J. Liu and C. Gan, "High-Frequency Voltage Injection Sensorless Control Technique for IPMSMs Fed by a Three-Phase Four-Switch Inverter With a Single Current Sensor," in *IEEE Trans. Ind. Electron.*, vol. 23, no. 2, pp. 758-768, April 2018.

[10] P. L. Xu and Z. Q. Zhu, "Novel square-wave signal injection method using zero-sequence voltage for sensorless control of PMSM drives," *IEEE Trans. Ind. Electron.,* vol. 63, no. 12, pp. 7444-7454, Dec. 2016.

[11] Q. Tang, A. Shen, X. Luo, and J. Xu, "PMSM sensorless control by injecting HF pulsating carrier signal into ABC frame," *IEEE Trans. Power Electron.*, vol. 32, no. 5, pp. 3767-3776, May 2017.

[12] G. Xie, K. Lu, S. K. Dwivedi, J. R. Rosholm, and F. Blaabjerg, "Minimum-voltage vector injection method for sensorless control of PMSM for low-speed operations," *IEEE Trans. Power Electron.*, vol. 31, no. 2, pp. 1785-1794, Feb. 2016.

[13] X. Jin, R. Ni, W. Chen, F. Blaabjerg, and D. Xu, "High-frequency voltage-injection methods and observer design for initial position detection of permanent magnet synchronous machines," *IEEE Trans. Power Electron.*, vol. 33, no. 9, pp. 7971-7979, Sep. 2018.

[14] H. Zhang, W. Liu, Z. Chen, G. Luo, J. Liu, and D. Zhao, "Asymmetric space vector modulation for PMSM sensorless drives based on square-wave voltage-injection method," *IEEE Trans. Ind. Appl.*, vol. 54, no. 2, pp. 1425-1436, March-April 2018.

[15] P. L. Xu and Z. Q. Zhu, "Novel carrier signal injection method using zero-sequence voltage for sensorless control of PMSM drives," *IEEE Trans. Ind. Electron.,* vol. 63, no. 4, pp. 2053-2061, Apr. 2016.

[16] H. Zhan, Z. Q. Zhu, M. Odavic, and Y. Li, "A novel zero-sequence model-based sensorless method for open-winding PMSM with common dc bus," *IEEE Trans. Ind. Electron.,* vol. 63, no. 11, pp. 6777-6789, Nov. 2016.

[17] W. Xu, Y. Jiang, C. Mu, and F. Blaabjerg, "Improved nonlinear flux observer-based second-order SOIFO for PMSM sensorless control," *IEEE Trans. Power Electron.*, vol. 34, no. 1, pp. 565-579, Jan. 2019.

[18] D. Liang, J. Li, R. Qu, and W. Kong, "Adaptive second-order sliding-mode observer for PMSM sensorless control considering VSI nonlinearity," *IEEE Trans. Power Electron.*, vol. 33, no. 10, pp. 8994-9004, Oct. 2018.

[19] Y. Wang, X. Wang, W. Xie, and M. Dou, "Full-speed range encoderless control for salient-pole PMSM with a novel full-order SMO," *Energies*, vol. 11, no. 9, pp. 1-14, 2018.

[20] A. Andersson and T. Thiringer, "Motion sensorless IPMSM control using linear moving horizon estimation with Luenberger observer state feedback," *IEEE Trans. Transportation Electrification*, vol. 4, no. 2, pp. 464-473, June 2018.

[21] O. Aydogmus and S. Sünter, "Implementation of EKF based sensorless drive system using vector controlled PMSM fed by a matrix converter," *Int. J. Elec. Power & Energy Sys.*, vol. 43, no. 1, pp. 736-743, 2012.

[22] V. Smidl and Z. Peroutka, "Advantages of square-root extended Kalman filter for sensorless control of AC drives," *IEEE Trans. Ind. Electron.,* vol. 59, no. 11, pp. 4189-4196, Nov. 2012.

[23] Y. S. Kung, N. V. Quynh, N. T. Hieu, and J. M. Lin, "FPGA realization of sensorless PMSM speed controller based on extended Kalman filter," *Mathematical Problems in Eng.*, pp.1-13, 2013.

[24] Y. Shi, K. Sun, L. Huang, and Y. Li, "Online identification of permanent magnet flux based on extended Kalman filter for IPMSM drive with position sensorless control," *IEEE Trans. Ind. Electron.,* vol. 59, no. 11, pp. 4169-4178, Nov. 2012.

[25] O. C. Kivanc and S. B. Ozturk, "Sensorless PMSM drive based on stator feedforward voltage estimation improved with MRAS multiparameter estimation," *IEEE/ASME Trans. Mechatron.*, vol. 23, no. 3, pp. 1326-1337, June 2018

[26] G. Chen, S. Yang, Y. Hsu, *et al.*, "Position and speed estimation of permanent magnet machine sensorless drive at high speed using an improved phase-locked loop," *Energies*, vol. 10, no. 10, 2017.

[27] M. H. Bierhoff, "A general PLL-type algorithm for speed sensorless control of electrical drives," *IEEE Trans. Ind. Electron.,* vol. 64, no. 12, pp. 9253-9260, Dec. 2017.

[28] L. Tong, *et al.*, "An SRF-PLL-based sensorless vector control using the predictive deadbeat algorithm for the direct-driven permanent magnet synchronous generator," *IEEE Trans. Power Electron.*, vol. 29, no. 6, pp. 2837-2849, June 2014.

[29] M. Preindl and E. Schaltz, "Sensorless model predictive direct current control using novel second-order PLL observer for PMSM drive systems," *IEEE Trans. Ind. Electron.,* vol. 58, no. 9, pp. 4087-4095, Sept. 2011.

[30] S. Lin and W. Zhang, "An adaptive sliding-mode observer with a tangent function-based PLL structure for position sensorless PMSM drives," *Int. J. Elec. Power & Energy Sys.*, vol. 88, pp. 63-74, 2017.

[31] X. Song, B. Han, S. Zheng, and S. Chen, "A novel sensorless rotor position detection method for high-speed surface PM motors in a wide speed range," *IEEE Trans. Power Electron.*, vol. 33, no. 8, pp. 7083-7093, Aug. 2018.

[32] G. Zhang, G. Wang, D. Xu, and N. Zhao, "ADALINE-network-based PLL for position sensorless interior permanent magnet synchronous motor drives," *IEEE Trans. Power Electron.*, vol. 31, no. 2, pp. 1450-1460, Feb. 2016.

[33] X. Song, J. Fang, B. Han, and S. Zheng, "Adaptive compensation method for high-speed surface PMSM sensorless drives of EMF-based position estimation error," *IEEE Trans. Power Electron.*, vol. 31, no. 2, pp. 1438-1449, Feb. 2016.

[34] I. P. T. Lanza, Y. B. Shtessel, and J. L. Stensby, "Improved acquisition in a phase-locked loop using sliding mode control techniques," *J. the Franklin Institute*, vol. 352, no. 10, 2015.

[35] X. Zhang and K. Wang, "Current prediction based zero sequence current suppression strategy for the semicontrolled open-winding PMSM generation system with a common dc bus," *IEEE Trans. Ind. Electron.,* vol. 65, no. 8, pp. 6066-6076, Aug. 2018.

[36] Y. Zhang, D. Xu, and L. Huang, "Generalized multiple-vector-based model predictive control for PMSM drives," *IEEE Trans. Ind. Electron.,* vol. 65, no. 12, pp. 9356-9366, Dec. 2018.
[37] H. T. Nguyen and J. Jung, "Finite control set model predictive control to guarantee stability and robustness for surface-mounted PM synchronous motors," *IEEE Trans. Ind. Electron.,* vol. 65, no. 11, pp. 8510-8519, Nov. 2018.
[38] M. Siami, D. A. Khaburi, M. Rivera, and J. Rodríguez, "A computationally efficient lookup table based FCS-MPC for PMSM drives fed by matrix converters," *IEEE Trans. Ind. Electron.,* vol. 64, no. 10, pp. 7645-7654, Oct. 2017.
[39] Z. Mynar, L. Vesely, and P. Vaclavek, "PMSM model predictive control with field-weakening implementation," *IEEE Trans. Ind. Electron.,* vol. 63, no. 8, pp. 5156-5166, Aug. 2016.
[40] X. Sun, et al., "MPTC for PMSMs of EVs with Multi-Motor Driven System Considering Optimal Energy Allocation." *IEEE Trans. Magn.*, vol. 55, no. 7, pp. 1-6, Jul. 2019.
[41] E. Trancho et al., "PM-Assisted Synchronous Reluctance Machine Flux Weakening Control for EV and HEV Applications," *IEEE Trans. Ind. Electron.,* vol. 65, no. 4, pp. 2986-2995, Apr. 2018.
[42] D. Nguyen, R. Dutta, M. F. Rahman and J. E. Fletcher, "Performance of a Sensorless Controlled Concentrated-Wound Interior Permanent-Magnet Synchronous Machine at Low and Zero Speed," *IEEE Trans. Ind. Electron.*, vol. 63, no. 4, pp. 2016-2026, Apr. 2016.
[43] Z. Wang, K. Lu, and F. Blaabjerg, "A simple startup strategy based on current regulation for back-EMF-based sensorless control of PMSM," *IEEE Trans. Power Electron.*, vol. 27, no. 8, pp. 3817-3825, Aug. 2012.

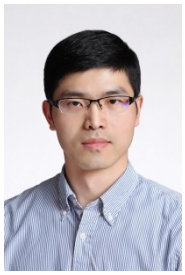

Xiaodong Sun (M'12-SM'18) received the B.Sc. degree in electrical engineering, and the M.Sc. and Ph.D. degrees in control engineering from Jiangsu University, Zhenjiang, China, in 2004, 2008, and 2011, respectively.

Since 2004, he has been with Jiangsu University, where he is currently a Professor with the Automotive Engineering Research Institute. From 2014 to 2015, he was a Visiting Professor with the School of Electrical, Mechanical, and Mechatronic Systems, University of Technology Sydney, Sydney, Australia. His current teaching and research interests include electrical machines and drives, drives and control for electric vehicles, and intelligent control. He is the author or coauthor of more than 80 refereed technical papers and one book, and he is the holder of 36 patents in his areas of interest.

Changchang Hu was born in Xuzhou, Jiangsu, China, in 1994. He received the B.S. degree in vehicle engineering from Jinling Institute of Technology, Nanjing, China, in 2017, and he is currently working toward the M.E. degree in Jiangsu University, Zhenjiang, China.

His current research interests include control of electrical drive systems and intelligent algorithm for automobile application.

Gang Lei (M'14) received the B.S. degree in Mathematics from Huanggang Normal University, China, in 2003, the M.S. degree in Mathematics and Ph.D. degree in Electrical Engineering from Huazhong University of Science and Technology, China, in 2006 and 2009, respectively. He is currently a senior lecturer at the School of Electrical and Data Engineering, University of Technology Sydney (UTS), Australia. His research interests include design optimization and control of electrical drive systems and renewable energy systems.

Zebin Yang received the B.Sc., M.Sc. and Ph.D. degrees in electrical engineering from Jiangsu University, Zhenjiang, China, in 1999, 2004, and 2013, respectively. where he is currently a professor in Jiangsu University. From 2014 to 2015, he was a Visiting Scholar with the School of Electrical, Mechanical, and Mechatronic Systems, University of Technology Sydney, Sydney, Australia. His main research interests include drives and control for bearingless motors and magnetic levitation transmission technology.

Youguang Guo (S'02-M'05-SM'06) received the B.E. degree from Huazhong University of Science and Technology, China in 1985, the M.E. degree from Zhejiang University, China in 1988, and the Ph.D. degree from University of Technology, Sydney (UTS), Australia in 2004, all in electrical engineering. He is currently a professor at the School of Electrical and Data Engineering, University of Technology Sydney (UTS). His research fields include measurement and modeling of properties of magnetic materials, numerical analysis of electromagnetic field, electrical machine design optimization, power electronic drives and control.

Jianguo Zhu (S'93–M'96–SM'03) received the B.E. degree in 1982 from Jiangsu Institute of Technology, Jiangsu, China, the M.E. degree in 1987 from Shanghai University of Technology, Shanghai, China, and the Ph.D. degree in 1995 from the University of Technology Sydney (UTS), Sydney, Australia, all in electrical engineering. He was appointed a lecturer at UTS in 1994 and promoted to full professor in 2004 and Distinguished Professor of Electrical Engineering in 2017. At UTS, he has held various leadership positions, including the Head of School for School of Electrical, Mechanical and Mechatronic Systems and Director for Centre of Electrical Machines and Power Electronics. In 2018, he joined the University of Sydney, Australia, as a full professor and Head of School for School of Electrical and Information Engineering. His research interests include computational electromagnetics, measurement and modelling of magnetic properties of materials, electrical machines and drives, power electronics, renewable energy systems and smart micro grids.